Evolution of surface structure in laser-preheated perturbed materials

C. A. Di Stefano,* E. C. Merritt, F. W. Doss, K. A. Flippo, A. M. Rasmus, and D. W. Schmidt
Los Alamos National Laboratory, Los Alamos, New Mexico 87501, USA
(Received 1 August 2016; revised manuscript received 15 December 2016; published 3 February 2017)

We report an experimental and computational study investigating the effects of laser preheat on the hydrodynamic behavior of a material layer. In particular, we find that perturbation of the surface of the layer results in a complex interaction, in which the bulk of the layer develops density, pressure, and temperature structure and in which the surface experiences instability-like behavior, including mode coupling. A uniform one-temperature preheat model is used to reproduce the experimentally observed behavior, and we find that this model can be used to capture the evolution of the layer, while also providing evidence of complexities in the preheat behavior. This result has important consequences for inertially confined fusion plasmas, which can be difficult to diagnose in detail, as well as for laser hydrodynamics experiments, which generally depend on assumptions about initial conditions in order to interpret their results.

DOI: 10.1103/PhysRevE.95.023202

I. INTRODUCTION

The phenomenon of preheating of components, primarily due to x rays or energetic particles produced by laser-material interactions [1–3], has long been a known complication of laser-driven, high-energy-density (HED) systems. This preheat can cause instability-like growth of structure at interfaces present in the system, which in turn alters the initial conditions and therefore complicates the analysis of processes that depend on those initial conditions. Existing studies of preheat typically focus either on quantifying the amount of energy deposited [4–7] and/or the transport mechanism [3,8] involved. Studies considering the subsequent interface dynamics themselves have either been computational [9–11] or have involved complex structure tailored to a specific application [12]. Further, these studies generally involve low-Z materials such as plastic, which are mostly transparent to typical preheat spectra, thereby minimizing the effect. In this work, we report the results of a combined computational and experimental study, studying a preheated interface of mid-Z composition (aluminum) that experiences significant energy deposition and therefore undergoes significant alteration of its initial conditions prior to the onset of other processes. This alteration of initial conditions is important for many experimental applications and is even more pronounced when higher-Z materials are involved due to their greater preheat absorption.

Fundamentally, the physical process underlying this evolution of the interface is the nonuniform expansion of the preheated material when its surface is perturbed and the consequent distortion of the perturbation features. The effect of preheat can, along these lines, be viewed as belonging to a family of Richtmyer-Meshkov and Rayleigh-Taylor-like processes [13,14] in that the underlying mechanism differs, but the resulting behavior of the system is similar. As a result of the preheat, the phase of the perturbation inverts, and small jets form in the troughs of any surface features of the preheated layer [15]. As we shall see below, this results in the evolution of new surface features, as a direct consequence of the preheating of the surface. It also results in the development of pressure and density gradients within the preheated layer, which will affect the layer's subsequent behavior under the action of shocks or other processes.

These physics are highly relevant to any laser-driven system in which there is a significant time delay between the initial laser pulse and the commencement of the physical processes of interest. For hydrodynamic instability of surface perturbations in typical HED systems, this time scale is typically one to a few nanoseconds. A particular example is the double-shell concept for the design of fuel capsules for inertial confinement fusion [16–20]. This scheme, employing two concentric spherical shells, adds considerable complexity to the capsule design, but inclusion of the second capsule may mitigate difficulties arising from issues such as drive asymmetry and convergence. Experiments exploring double-shell implosions using the indirect-drive approach have been carried out on virtually every generation of major pulsed laser system, starting with Shiva [21,22] and continuing through OMEGA-60 [16,23], and planned work at the National Ignition Facility (NIF) [24] is currently under development [20,25]. Double-shell capsules are also a possible option for the direct-drive approach [26–28], although preheat in this case behaves differently than with hohlraum indirect drive.

In a double-shell implosion, the outer capsule is irradiated and a few nanoseconds pass before the outer shell impacts the inner shell, transferring its kinetic energy. The inner shell then implodes and compresses the fuel. This scheme is theorized to mitigate the growth of hydrodynamic instability—an important problem for high-convergence, single-shell implosions—but a major concern is that preheating of the inner shell may amplify surface features and therefore seed significant instability growth after impact. Understanding the behavior of this preheat is critical to assessing the viability of the double-shell idea.

Further, virtually any HED shock-driven hydrodynamics experiment will involve this kind of preheat effect, because they generally require one to irradiate a particular surface and then wait some amount of time for a shock to form and propagate to another location [9,29–36]. These systems often involve a material interface with seeded interface structure, and it is often assumed or approximated that the prefabricated initial

*carlosds@lanl.gov

conditions and the conditions encountered by the shock are identical. This is not necessarily valid [37] and a more thorough understanding of how initial conditions evolve is important in correctly interpreting the results of these experiments. For instance, the work presented here is part of a larger experimental effort investigating shear instability in a geometry involving counterpropagating flows [38,39]. The flow consists of two shocks in a low-density CH foam, driven in opposite directions by laser ablation, on either side of an aluminum collimating layer. When the shocks cross at the center of the system, a shear layer with laterally balanced pressure forms, and the experiment seeks to understand the evolution of the layer. The Al layer is easy to manipulate and can be seeded with a range of initial conditions, including the two-dimensional (2D) single-mode sinusoids described in this work.

When the lasers irradiate the system, they preheat the Al, and the evolution of the preheated Al dictates the initial conditions for shear instability experienced by the shocks. In particular, we find two main effects. First, the Al undergoes a bulk expansion due to the increased pressure caused by the preheat preferentially being deposited in this layer. Second, any surface perturbation causes the development of density and pressure gradients within the Al, as well as the formation of jets in the troughs of any surface features, leading to evolution of the initial surface structure. We focus on studying the latter in this work.

II. EXPERIMENTAL SYSTEM AND RESULTS

The experimental system is constructed by first coining a rectangular Al foil, nominally 20 μm thick, such that a sinusoidal perturbation of nominal initial amplitude $a_o = 2.74 \pm 0.85$ μm and of a given wavelength is impressed on both sides [40]. These wavelengths range from 50 μm to 200 μm. A semicylindrical piece of carbon foam of density 0.06 g/cm^3 is then placed against either face of the foil, such that the assembly forms a cylinder of radius 250 μm and length 1.55 mm. Finally, a semicylindrical piece of gold is placed at one end of each piece of foam. The purpose of this gold is to prevent the shock from propagating into its half of the cylinder. The entire assembly is then inserted into a 100-μm-thick Be tube, and 75-μm-thick polystyrene ablators are placed over each end. A sketch of the system is shown in Fig. 1.

Each ablator is simultaneously irradiated by a 1-ns OMEGA-60 laser pulse, each with a uniform intensity on the ablator of approximately 10^{15} W/cm^2 and a flat-topped profile in time. This is accomplished by overfilling the ablator with a laser spot size of full width at half maximum of about 500 μm and containing 4 kJ of total energy, such that the super-Gaussian profile of the spot does not begin to fall off within the region of interest. Laser energy outside of the region of interest is blocked by a conical gold shield coated with parylene. The laser pulses drive the counterpropagating shocks previously mentioned but also preheat the Al foil, increasing its temperature and pressure, and causing it to noticeably expand. This preheat is asymmetric, since the asymmetrically placed gold shock blockers will attenuate it in opposite hemicylinders in each half of the system, but near the center the two preheat sources are irradiating opposite sides of the foil from approximately equal perspectives. Therefore, we expect roughly symmetric preheat there.

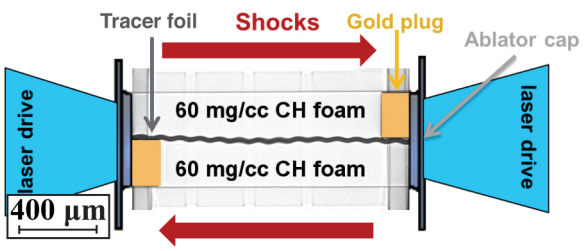

FIG. 1. Sketch of the experimental system. Lasers irradiate the system from both ends, driving a left-propagating shock in the top half and a right-propagating shock in the bottom half. The thickness and surface shape of the tracer foil near the center is the primary measurement of interest.

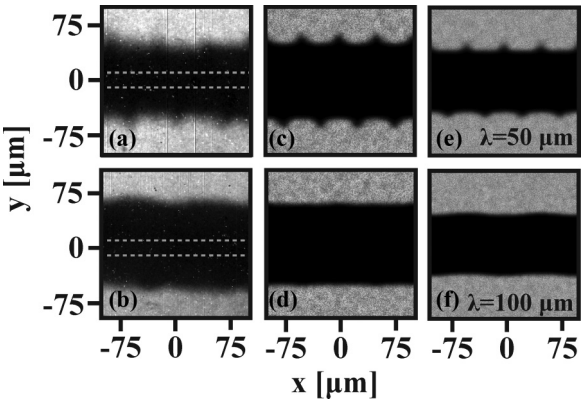

FIG. 2. [(a) and (b)] Examples of experimental images taken at $t = 6$ ns, with $\lambda = 50$ μm and $\lambda = 100$ μm, showing evolution of the sinusoidal perturbation, with the initial foil thickness shown by the dashed lines; [(c) and (d)] simulated radiographs of the same systems, with the Al at an initial temperature of 2.25 eV; [(e) and (f)] simulated radiographs of the same systems, with the Al at an initial temperature of 1.5 eV.

The driven shocks flow transverse to the surface of the foil, and the preheat experiment ends at each given location of the foil as the shock passes, at which time shear flow becomes the main process responsible for further evolution of the foil [38,41]. The experiment is diagnosed by point-projection backlit radiography, employing a scandium He-α source (4.3 keV photons) behind a 20-μm-diameter aperture with 24$\times$ magnification. This signal is received by a microchannel plate gated to 200 ps, which converts the x rays into visible light, producing an image on a charge-coupled-device detector.

Examples of data taken at 6 ns, with 50- and 100-μm seeds, are shown in Figs. 2(a) and 2(b), respectively. In these frames, the foil is the dark central layer, and the surrounding light regions correspond to the CH foam. For reference, the nominal 20-μm initial thickness of the foil is shown as dotted gray lines, which clearly demonstrates the bulk expansion of the foil under the laser preheat of the system. The initial perturbation amplitudes for these foils is as follows: in Fig. 2(a), the top and bottom surfaces have $a = 2.4$ μm and $a = 4.4$ μm, respectively, and in Fig. 2(b), the top and bottom surfaces have $a = 3.3$ μm and $a = 3.0$ μm, respectively. The qualitative

difference in surface morphology between the two cases is evident, and we turn to simulations to study in more detail how this occurs.

Finally, because the diagnostic is line-of-sight integrated, we briefly discuss the influence of small misalignments of the Al layer with respect to the imaging plane. Alignment, to the imaging plane, of the foil layer about the tube axis (up or down in the imaging plane) is done to within 0.5°, which would correspond to an apparent increase of the thickness of the Al layer of less than 7 μm if the Al was completely opaque. Since this is not the case (for example, 10 μm of full-density, solid aluminum attenuates would attenuate about half of the 4.3-keV imaging x rays, and we expect the aluminum to decompress significantly as it expands), we believe that the maximum error this introduces is in reality less than 7 μm. Further, since we do not expect edge effects at the tube-foil interface to be significant until the system is shocked, we expect that the misalignment effect would at worst lead to minor blurring of the interface rather than loss of visibility of the structure. The sinusoidal perturbation is also aligned to within a few tenths of a degree of the foil edge. We again expect this to have at most a minor blurring effect on the features, without losing any of the structure.

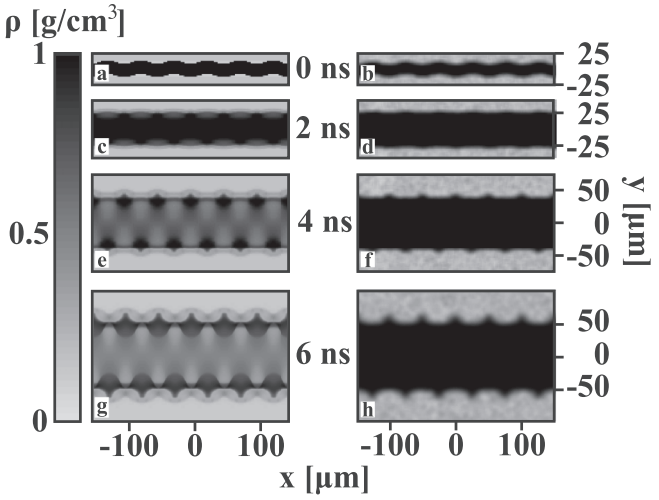

FIG. 3. Time sequence of the simulated system, with $\lambda = 50$ μm and $T_{Al} = 2.25$ eV. Left column: Density maps, showing the formation of jets via accumulation of material into the sinusoidal troughs; right column: simulated radiographs, predicting the final appearance of the data. Note that the only detail visible should be the overall contour of the interface.

III. COMPUTATIONAL RESULTS

In order to investigate the preheat effect in more detail, we performed hydrodynamic simulations of the system using the 2D RAGE [42] code. The simulations were set up using a 20-μm-thick layer, using a SESAME equation of state (EOS) including thermal conductivity for aluminum, with a superposed single-mode sinusoidal perturbation on each side. The amplitudes and wavelengths used were those corresponding to pre-experiment measurements made on the foils using a Zygo optical surface profiler [43]. This layer was surrounded by foam, modeled as low-density polystyrene, in a domain sufficiently large to allow the system to evolve for 9 ns, past the times of interest for preheat evolution. Finally, the aluminum layer was seeded with a uniform temperature at time $t = 0$ ns and allowed to evolve. Because the preheat is preferentially deposited in the higher-Z aluminum rather than the lower-Z foam made predominantly of carbon and hydrogen, we chose to approximate the foam as being initially cold.

The simulated aluminum then experiences, over time, a bulk expansion due to its increased pressure, and also exhibits the formation of aluminum jets in the troughs of the original sinusoids. We find that an initial aluminum temperature of $T_{Al} = 2.25$ eV best reproduces the observed time rate of bulk expansion of the foil. The accuracy in system alignment, as discussed in Sec. II, introduces a maximum apparent increase in bulk thickness that can be accounted for by about a 0.2-eV reduction in source temperature, so the final value is $T_{Al} = 2.15 \pm 0.1$ eV. Meanwhile, we will see that a lower initial temperature, of $T_{Al} = 1.5 \pm 0.25$ eV, better reproduces the evolution of the surface structure, where the reported error corresponds to the temperature variation that would reproduce the uncertainty in our amplitude measurements. Simulated radiographs, corresponding to the data shown in Figs. 2(a) and 2(b), are shown in Figs. 2(c) and 2(d), respectively. In these frames, we see that the simulation has reproduced the bulk thickness of the layer. Finally, Figs. 2(e) and 2(f) show simulated radiographs using a lower initial temperature of $T_{Al} = 1.5$ eV. This lower temperature is required to better reproduce the time rate of jet formation, which is hardly visible at all in the simulation employing the higher temperature. Results from these simulations will be discussed below.

A characteristic of our imaging diagnostic is that it obscures any structure present within the aluminum in order to maximize the contrast seen at the Al-foam interface. Therefore, we turn to the density maps produced by the simulation in order to understand how the experimentally observed structure develops. The left column of Fig. 3 shows a time sequence of simulated density maps, for the $\lambda = 50$ μm and $T_{Al} = 2.25$ eV case, in which darker color represents areas of higher density, while lighter color represents areas of lower density. As the preheated system is allowed to evolve, we see that the pressure imbalance between the preheated Al and the cold foam has launched a lateral shock off the surface of the Al that propagates into the foam, while the average thickness of the Al layer is increasing. Meanwhile, between 0 and 2 ns, it is evident that Al is accumulating in the areas that initially corresponded to the troughs of the seed sinusoid. By 4 ns, the original sinusoid has inverted, and the surface structure now consists of small jets that have formed in the sinusoidal troughs. The right column of Fig. 3 shows simulated radiographs corresponding to the density maps in the left column. These simulated radiographs clearly show that we expect to see neither the density structure in the Al nor the lateral shocks in the foam. These density gradients, and their corresponding temperature and pressure gradients, can have important effects on the further behavior of the materials, yet even in a simple Cartesian geometry such as ours, they can be very difficult to diagnose.

These simulated images do, however, allow us to interpret the features we see in the data. Note the difference in

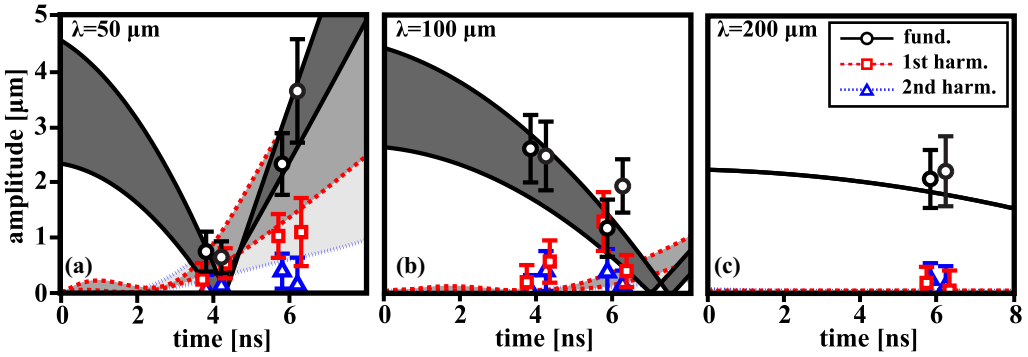

FIG. 4. Measurements of the growth rate for the simulation (curves), with an initial foil temperature of $T_{\mathrm{Al}} = 1.5$ eV and the data (points). Note that data points are slightly offset along the abscissa for visibility and that the two measurements for a given wavelength and imaging time correspond to the two sides of the foil. Each pair of curves of a single style corresponds to the simulated growth arising from the largest and smallest initial experimental amplitudes. The corresponding gray bands show the amplitude space they demarcate. Solid black corresponds to the fundamental mode, dashed red to the first harmonic, and dotted blue to the second harmonic. The phase of the first harmonic reverses as the jets begin to appear, while the phase of the fundamental reverses as the jets become taller than the sinusoidal peaks. These occur when the amplitudes of the two modes hit zero, at about 2.5 and 4 ns in frame a ($\lambda = 50$ μm), and at about 4 and 7 ns in frame b ($\lambda = 100$ μm). (a) $\lambda = 50$ μm; (b) $\lambda = 100$ μm; (c) $\lambda = 200$ μm.

appearance between the features in Fig. 3(b); the original perturbation clearly shows the sinusoidal shape impressed on the foil during fabrication. This is in contrast with Fig. 3(h), where the jets have a squarelike appearance. These differences, once understood from the simulation, are identifiable in the data at all wavelengths. Further, the simulated radiograph allows us to understand how a small amount of foil misalignment can cause the squarish appearance of the jet, as can be seen by comparison between Fig. 3(g) and Fig. 3(h).

IV. DISCUSSION

The production of jets clearly alters the initially seeded sinusoidal structure of the interface, and we find that mode coupling affects the spectral content of the interface, not just the amplitudes of the features. This can be seen from measurements of the interface for three perturbation wavelengths, made from both the data and the simulations, which are shown in Fig. 4. In Fig. 4, the experimental amplitudes were measured in a manner similar to that reported in Refs. [44,45], with the caveat that in this case, the aluminum layer is very thick and very opaque. Therefore, in a transmission radiograph, the contour corresponding to the mean Al-foam interface will be at a signal level close to that of the dark Al, and the measurements were made accordingly. To obtain the simulated amplitudes, we initialized the simulation with the sinusoidal amplitudes of the actual foils used in the experiment and tuned the preheat to $T_{\mathrm{Al}} = 1.5$ eV in order to match the simulated amplitudes to the experimental measurements.

The initial amplitudes of the foils were obtained by acquiring surface scans of the foils using a profilometer and then using Fourier analysis to measure the amplitudes. These amplitudes, along with the time at which each foil was imaged, are tabulated in Table I, and it can be seen from the table that there was significant variation in the initial amplitudes of the experimental foils resulting from the coining process. Further, it was not clear from pre-experiment metrology which way the foils were oriented in the experiment. Therefore, we repeated the simulation with the range of initial amplitudes corresponding to each case in order to ensure that the simulated results show the variation possible from the experimental initial conditions. This variation appears as the bands in Fig. 4, which bound the possible growth predicted by the simulation for the experimental foils. Examples of the simulated radiographs generated using this preheat temperature were previously shown in Fig. 2(e) and 2(f).

The physical interpretation of Fig. 4 is as follows. Initially, the amplitude of the fundamental mode corresponds to the height of the sinusoidal peaks, which decreases in amplitude as the foil expands and the material that will become the jets accumulates near the troughs. This effect is also evident in Figs. 3(a)–3(d). The first harmonic, in phase with the fundamental, appears as a modulation to the shape of the sinusoid. As the jets begin to appear in the sinusoidal troughs, the first harmonic reverses phase, as it is now representing the combination of the jets and the remnants of the sinusoidal peaks. This is indicated by the amplitude of the first harmonic approaching zero (at approximately 2.5 ns for $\lambda = 50$ μm and at approximately 4 ns for $\lambda = 100$ μm). Subsequently, the jets grow as the sinusoid shrinks, and when the two features have the same amplitude, the fundamental mode vanishes. This can

TABLE I. Initial perturbation amplitudes for the foils used in the experiments, obtained by Fourier analysis of surface scans of the foils, along with the perturbation wavelength and the imaging time. The approximate feature-to-feature size variation within a given foil was ± 0.2 μm.

λ (μm)	Time (ns)	Amplitude (μm)	
50	4	2.3	3.1
50	6	2.4	4.4
100	4	2.6	4.3
100	6	3.0	3.3
200	6	2.2	2.2

be thought of as the interface inversion time. After this time, the fundamental mode reappears, also with a phase shift of 180°, as its peaks now correspond to the larger jet peaks instead of the sinusoidal peaks. Higher harmonics are also present, but are not as easy to visualize, as their role is to introduce small deformations in the curvature of the structure, but they do not correspond to any new features. These modes are in phase with the first two following reversal. Comparison of the three wavelengths shown in Figs. 4(a)–4(c) indicates that the structure evolves more slowly for longer wavelengths, and by the time the wavelength reaches $\lambda = 200$ μm, little of interest happens within the experimental time scale.

The latter case, shown in Fig. 4(c), also serves to corroborate our reasoning that experimental misalignment does not significantly affect our measurements. The simulation suggests that the time scale is not sufficient for the surface perturbation to evolve, and the measurement from the data produces the correct single mode and an amplitude within the bounds of uncertainty of the measured initial amplitude. This leads us to conclude that the measurement technique is valid.

It is apparent from Fig. 4 that the original seeded mode has the largest postinversion growth rate (indicating that the jet is the dominant physical process), but the interface retains its multimode nature. The exact behavior, including the appearance of harmonics, the inversion time, and the relative postinversion amplitudes of the modes depend primarily on the initial wavelength and the preheated temperature. This behavior depends to a lesser extent on the initial amplitudes. For example, for a given temperature and initial amplitude, the simulated inversion time depends on the wavelength in an approximately linear fashion. This hold true so long as the initial amplitude is small compared to the wavelength, and is reasonable from dimensional arguments, since the main quantities of interest are the temperature T, the wavelength λ, and the inversion time τ. One can construct a nondimensional quantity from these parameters, in which allowing T to enter the expression through the sound speed for a plasma gives further insight for how the effect might change if we were to substitute other elements for aluminum. (Though this has not been done with the present experiment, it has been done for the NIF analog [46].) The easiest way to visualize the result is to approximate the EOS of the Al plasma as that of a polytropic ideal gas, with the resulting expression being

$$\frac{\gamma(1+Z)k_BT}{Am_p}\frac{\tau^2}{\lambda^2}. \tag{1}$$

In this expression, k_B is the Boltzmann constant, γ and Z are the polytropic index and ionization state of the plasma, A is the mass number of the foil, and m_p is the proton mass. Similar relationships can be constructed for the postinversion modal growth rates and for the amplitude of the fundamental mode at the crossing time of the shocks. So, we see that the inversion time will vary approximately linearly with wavelength, and as the $-\frac{1}{2}$ power of the temperature. An understanding of the behavior of these quantities for a given system brings useful knowledge to the planning and interpretation of experiments in which the preheat process affects subsequent dynamics. For example, although there is a transient period before the amplitude growth reaches its linear growth rate, the above relation could be used to estimate how variation of the initial conditions might affect the results if at least one data point is already in hand.

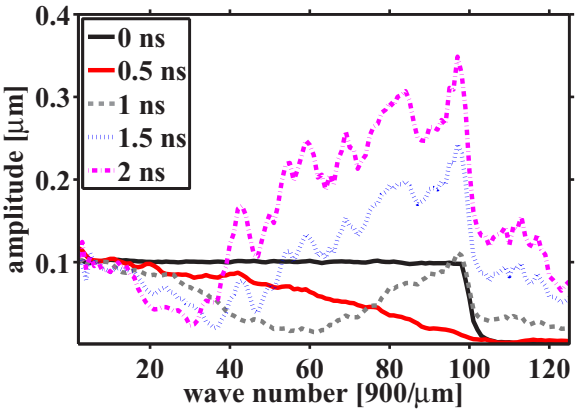

FIG. 5. The simulated surface spectrum of a foil with a white-noise initial perturbation, sampled at various times. The shift of the wave number of inverting modes with time is evident from the plots.

We now briefly discuss the manifestation of this preheat behavior when the initial surface structure is multimodal in nature. This kind of situation arises, for example, with roughened surfaces [47], where the initial spectrum often obeys the relation $a_o \propto k^{-1}$. To this end, we performed a similar computation with the simpler white-noise power spectrum, results from which are shown in Fig. 5. These simulations are identical to the single-mode simulations described earlier, except the foil was seeded with a nominal temperature $T_{Al} = 2$ eV. In the figure, the initial spectrum is shown as the black curve, where the initial modal amplitudes are $a_o = 0.1$ μm on the range $\ell = [1,100]$, where $\ell \equiv 900/\lambda$, and $a_o = 0$ elsewhere. The results indicate, as one might expect, that similar mode behavior occurs as in the single-sinusoid case even without specific features to correspond to any given mode, except with the spectrum the time scales tend to continuous transitions. At $t = 0.5$ ns, shorter wavelengths are more flattened, while in the long-wavelength limit, the change asymptotically approaches zero. As time progresses, the modes experience their phase inversion in decreasing order of wave number, while their amplitudes have similar growth rates far from the long-wavelength limit. Meanwhile, the modes $\ell > 100$ experience growth as the harmonics of the seeded modes. We also note that the wavelengths at which phase inversion is occurring at any given time, identifiable by the inflection in the spectrum, also shows the approximately linear progression in time, as was observed in the single-mode case.

A practical conclusion suggested by this analysis is that if the amount of time the system has to preheat is short (an equivalent situation to one in which the amount of preheat is low), then the longer wavelengths in the system, at approximately their initial amplitudes, will dominate as the main seed for instability. In contrast, if the system is allowed to preheat for a longer time, then the influence of the shorter wavelengths will become stronger due to their faster initial growth. This is the relevant case for many of the examples presented in Sec. I, implying that pre-experiment measurement of the initial surface conditions is not sufficient

for understanding the instability seed. This analysis could also be a useful tool in connecting the growth of large-scale features, which can be directly observed, and smaller-scale mixing that is typically broadband in nature and can only be simulated using statistical models of material mixing.

Finally, we again note that the one-temperature model used in this work is capable of reproducing both the bulk expansion and the growth of surface structure on the foil but not simultaneously using the same modeled energy. Some of the difference (2.15 ± 0.1 eV and 1.5 ± 0.25 eV, respectively) could be explained by uncertainty in the measurements of the bulk thickness and feature size of the foil, but this is probably not sufficient to fully account for it. Although the compatibility of these numbers is weak, they do seem persistent enough to warrant further investigation. The kind of analysis presented here could be used to probe the higher-order details of the physics of preheat absorption, including the composition of the x-ray and particle spectra of the preheat, by using multiple temperature models capable of matching the separate processes simultaneously. Such analysis can be useful in planning and interpreting future experiments, since the content of these spectra is highly variable according to the irradiation conditions of a particular experiment, and the consequences of the preheat are also variable according to the material composition of the experimental system. One possibility is to intentionally engineer initial conditions in order to produce a particular profile at a specific time. Another is to understand what effect a preheat mitigation scheme, if feasible, would have.

V. CONCLUSIONS

In summary, the results of this study indicate a significant influence of preheat on the initial conditions of laser-driven experiments. Perturbation of the surface of a preheated material will cause the formation of jets at the surface, as well as the development of a related, complex structure of gradients within the material. We have shown, for the case of a single mode, how this surface structure depends on the amount of preheat, the perturbation mode, and the time delay between the deposition of preheat energy and the onset of the primary process being driven in the experiment. More-complex surface structure will result in a more-complex preheat effect, as the jets will form of varying sizes and develop on varying time scales, and the gradients in the bulk material will also be more complicated. These effects are relevant to any system that relies on the uniformity or the ability to characterize the profile of the preheated material, such as the double-shell work and laser-driven hydrodynamics experiments discussed previously, which can depend on the assessment of preheat in order to understand the conditions under which those systems operate. These conditions include the seeding of hydrodynamic instability. A specific example is the counterpropagating shear experiment whose platform was used to perform this study. Correctly tracking the early-time effect of preheat on the initial conditions of that experiment is crucial to correctly applying the late-time results in testing our theoretical and computational understanding of the behavior of shear instability.

ACKNOWLEDGMENTS

The authors thank the facility staff at the Laboratory for Laser Energetics, as well as the MST-7 target fabrication team at Los Alamos, and Paul Bradley. This work was performed under the auspices of the U.S. Department of Energy by Los Alamos National Laboratory under Contract No. DE-AC52-06NA25396.

[1] B. Yaakobi, I. Pelah, and J. Hoose, Phys. Rev. Lett. **37**, 836 (1976).
[2] J. D. Lindl, *Inertial Confinement Fusion* (American Institute of Physics Press, New York, NY, 1998).
[3] H. Shu, S. Fu, X. Huang, J. Wu, Z. Xie, F. Zhang, J. Ye, G. Jia, and H. Zhou, Phys. Plasmas **21**, 082708 (2014).
[4] B. Yaakobi, C. Stoeckl, T. Boehly, D. D. Meyerhofer, and W. Seka, Phys. Plasmas **7**, 3714 (2000).
[5] B. Yaakobi, C. Stoeckl, W. Seka, J. A. Delettrez, T. C. Sangster, and D. D. Meyerhofer, Phys. Plasmas **12**, 062703 (2005).
[6] F. W. Doss, H. F. Robey, R. P. Drake, and C. C. Kuranz, Phys. Plasmas **16**, 112705 (2009).
[7] C. Kuranz, F. Doss, R. Drake, M. Grosskopf, and H. Robey, High Energy Density Phys. **6**, 215 (2010).
[8] C. C. Kuranz, R. P. Drake, K. K. Dannenberg, P. J. Susalla, D. J. Kremer, T. Boehly, and J. Knauer, Astrophys. Space Sci. **298**, 267 (2004).
[9] A. R. Miles, D. G. Braun, M. J. Edwards, H. F. Robey, R. P. Drake, and D. R. Leibrandt, Phys. Plasmas **11**, 3631 (2004).
[10] Y. Zhang, R. P. Drake, J. Glimm, J. W. Grove, and D. H. Sharp, Nonlinear Analysis: Theory, Methods, and Applications **63**, e1635 (2005).
[11] Y. Zhang, R. P. Drake, and J. Glimm, Phys. Plasmas **14**, 062703 (2007).
[12] N. E. Lanier, J. Workman, R. L. Holmes, P. Graham, and A. Moore, Phys. Plasmas **14**, 056314 (2007).
[13] A. L. Velikovich, J. P. Dahlburg, A. J. Schmitt, J. H. Gardner, L. Phillips, F. L. Cochran, Y. K. Chong, G. Dimonte, and N. Metzler, Phys. Plasmas **7**, 1662 (2000).
[14] Y. Aglitskiy, A. L. Velikovich, M. Karasik, N. Metzler, S. T. Zalesak, A. J. Schmitt, L. Phillips, J. H. Gardner, V. Serlin, J. L. Weaver, and S. P. Obenschain, Philos. Trans. Roy. Soc. Lond. A **368**, 1739 (2010).
[15] Y. Aglitskiy, M. Karasik, A. L. Velikovich, V. Serlin, J. L. Weaver, T. J. Kessler, S. P. Nikitin, A. J. Schmitt, S. P. Obenschain, N. Metzler, and J. Oh, Phys. Plasmas **19**, 102707 (2012).
[16] W. S. Varnum, N. D. Delamater, S. C. Evans, P. L. Gobby, J. E. Moore, J. M. Wallace, R. G. Watt, J. D. Colvin, R. Turner, V. Glebov, J. Soures, and C. Stoeckl, Phys. Rev. Lett. **84**, 5153 (2000).
[17] P. Amendt, J. D. Colvin, R. E. Tipton, D. E. Hinkel, M. J. Edwards, O. L. Landen, J. D. Ramshaw, L. J. Suter, W. S. Varnum, and R. G. Watt, Phys. Plasmas **9**, 2221 (2002).

[18] P. Amendt, R. E. Turner, and O. L. Landen, Phys. Rev. Lett. **89**, 165001 (2002).
[19] H. F. Robey, T. S. Perry, H.-S. Park, P. Amendt, C. M. Sorce, S. M. Compton, K. M. Campbell, and J. P. Knauer, Phys. Plasmas **12**, 072701 (2005).
[20] H. F. Robey, P. A. Amendt, J. L. Milovich, H.-S. Park, A. V. Hamza, and M. J. Bono, Phys. Rev. Lett. **103**, 145003 (2009).
[21] D. R. Speck, E. S. Bliss, J. A. Glaze, J. W. Herris, F. W. Holloway, J. T. Hunt, B. C. Johnson, D. J. Kuizenga, R. G. Ozarski, H. G. Patton *et al.*, IEEE J. Quant. Electron. **17**, 1599 (1981).
[22] H. Ahlstrom, Appl. Opt. **20**, 1902 (1981).
[23] T. R. Boehly, R. S. Craxton, T. H. Hinterman, J. H. Kelly, T. J. Kessler, S. A. Kumpan, S. A. Letzring, R. L. McCrory, S. F. B. Morse, W. Seka, S. Skupsky, J. M. Soures, and C. P. Verdon, Rev. Sci. Instrum. **66**, 508 (1995).
[24] E. I. Moses, J. Phys.: Conf. Ser. **112**, 012003 (2008).
[25] J. L. Milovich, P. Amendt, M. Marinak, and H. Robey, Phys. Plasmas **11**, 1552 (2004).
[26] B. Canaud, S. Laffite, and M. Temporal, Nucl. Fusion **51**, 062001 (2011).
[27] G. A. Kyrala, N. D. Delamater, D. C. Wilson, J. A. Guzik, D. A. Haynes, M. Gunderson, K. A. Klare, R. W. Watt, W. M. Wood, and W. S. Varnum, Laser Part. Beams **23**, 187 (2005).
[28] G. A. Kyrala, M. A. Gunderson, N. D. Delamater, D. A. Haynes, D. C. Wilson, J. A. Guzik, and K. A. Klare, Phys. Plasmas **13**, 056306 (2006).
[29] X. Fleury, S. Bouquet, C. Stehlé, M. Koenig, D. Batani, A. Benuzzi-Mounaix, J.-P. Chièze, N. Grandjouan, J. Grenier, T. Hall, E. Henry, J.-P. Lafon, S. Leygnac, V. Malka, B. Marchet, H. Merdji, C. Michaut, and F. Thais, Laser Part. Beams **20**, 263 (2002).
[30] S. G. Glendinning, J. Bolstad, D. G. Braun, M. J. Edwards, W. W. Hsing, B. F. Lasinski, H. Louis, A. Miles, J. Moreno, T. A. Peyser, B. A. Remington, H. F. Robey, E. J. Turano, C. P. Verdon, and Y. Zhou, Phys. Plasmas **10**, 1931 (2003).
[31] E. C. Harding, J. F. Hansen, O. A. Hurricane, R. P. Drake, H. F. Robey, C. C. Kuranz, B. A. Remington, M. J. Bono, M. J. Grosskopf, and R. S. Gillespie, Phys. Rev. Lett. **103**, 045005 (2009).
[32] O. A. Hurricane, V. A. Smalyuk, K. Raman, O. Schilling, J. F. Hansen, G. Langstaff, D. Martinez, H.-S. Park, B. A. Remington, H. F. Robey, J. A. Greenough, R. Wallace, C. A. Di Stefano, R. P. Drake, D. Marion, C. M. Krauland, and C. C. Kuranz, Phys. Rev. Lett. **109**, 155004 (2012).
[33] V. A. Smalyuk, J. F. Hansen, O. A. Hurricane, G. Langstaff, D. Martinez, H.-S. Park, K. Raman, B. A. Remington, H. F. Robey, O. Schilling, R. Wallace, Y. Elbaz, A. Shimony, D. Shvarts, C. Di Stefano, R. P. Drake, D. Marion, C. M. Krauland, and C. C. Kuranz, Phys. Plasmas **19**, 092702 (2012).
[34] G. Malamud, C. A. D. Stefano, Y. Elbaz, C. Huntington, C. C. Kuranz, P. A. Keiter, and R. P. Drake, High Energy Density Phys. **9**, 122 (2013).
[35] C. A. Di Stefano, G. Malamud, C. C. Kuranz, S. R. Klein, C. Stoeckl, and R. P. Drake, Appl. Phys. Lett. **106**, 114103 (2015).
[36] W. C. Wan, G. Malamud, A. Shimony, C. A. Di Stefano, M. R. Trantham, S. R. Klein, D. Shvarts, C. C. Kuranz, and R. P. Drake, Phys. Rev. Lett. **115**, 145001 (2015).
[37] C. A. Di Stefano, G. Malamud, M. T. Henry de Frahan, C. C. Kuranz, A. Shimony, S. R. Klein, R. P. Drake, E. Johnsen, D. Shvarts, V. A. Smalyuk, and D. Martinez, Phys. Plasmas **21**, 056306 (2014).
[38] F. Doss, E. Loomis, L. Welser-Sherrill, J. Fincke, K. Flippo, and P. Keiter, Phys. Plasmas (1994-present) **20**, 012707 (2013).
[39] F. W. Doss, J. L. Kline, K. A. Flippo, T. S. Perry, B. G. DeVolder, I. Tregillis, E. N. Loomis, E. C. Merritt, T. J. Murphy, L. Welser-Sherrill, and J. R. Fincke, Phys. Plasmas **22**, 056303 (2015).
[40] D. Capelli, D. W. Schmidt, T. Cardenas, G. Rivera, R. B. Randolph, F. Fierro, E. C. Merritt, K. A. Flippo, F. W. Doss, and J. L. Kline, Fusion Sci. Technol. **70**, 316 (2016).
[41] E. C. Merritt, F. W. Doss, E. N. Loomis, K. A. Flippo, and J. L. Kline, Phys. Plasmas **22**, 062306 (2015).
[42] M. Gittings, R. Weaver, M. Clover, T. Betlach, N. Byrne, R. Coker, E. Dendy, R. Hueckstaedt, K. New, W. R. Oakes, D. Ranta, and R. Stefan, Comput. Sci. Discov. **1**, 015005 (2008).
[43] http://www.zygo.com/?/met/profilers/opticalprofilersabout.htm.
[44] G. Malamud, A. Shimony, W. C. Wan, C. A. D. Stefano, Y. Elbaz, C. C. Kuranz, P. A. Keiter, R. P. Drake, and D. Shvarts, High Energy Density Phys. **9**, 672 (2013).
[45] C. A. Di Stefano, G. Malamud, C. C. Kuranz, S. R. Klein, and R. P. Drake, High Energy Density Phys. **17, Part B**, 263 (2015).
[46] F. W. Doss, K. A. Flippo, and E. C. Merritt, Phys. Rev. E **94**, 023101 (2016).
[47] K. A. Flippo, F. W. Doss, J. L. Kline, E. C. Merritt, D. Capelli, T. Cardenas, B. DeVolder, F. Fierro, C. M. Huntington, L. Kot, E. N. Loomis, S. A. MacLaren, T. J. Murphy, S. R. Nagel, T. S. Perry, R. B. Randolph, G. Rivera, and D. W. Schmidt, Phys. Rev. Lett. **117**, 225001 (2016).